A one year sea surface heat budget in the Northeastern Atlantic basin during the POMME experiment. Part II: Flux correction

Guy Caniaux, Sophie Belamari, Hervé Giordani, A. Paci, Louis Prieur, Gilles Reverdin

A 1 year sea surface heat budget in the northeastern Atlantic basin during the POMME experiment: 2. Flux optimization

G. Caniaux, S. Belamari, H. Giordani, and A. Paci
Centre National de Recherches Météorologiques, Toulouse, France

L. Prieur
Laboratoire d'Océanographie de Villefranche-sur-mer, Villefranche-sur-mer, France

G. Reverdin
Laboratoire d'Océanographie et du Climat: Expérimentation et Approche Numérique, Institut Pierre Simon Laplace, Paris, France

Received 1 September 2004; revised 16 February 2005; accepted 8 March 2005; published 2 July 2005.

[1] Gridded air-sea fluxes were computed during a 1 year period by applying a synthesis approach (Caniaux et al., 2005) as part of the Programme Océan Multidisciplinaire Méso Echelle (POMME) (September 2000–October 2001 in the northeast Atlantic 21°–15°W, 38°–45°N). In the present paper we address the question of adjusting the precipitation and turbulent surface fluxes so that the corresponding heat, salt, and momentum budgets are in agreement with the evolution of the thermal and salt contents deduced from the data collected during the experiment. The proposed method is based on the one-dimensional modeling of the whole POMME area by solving specific temperature and salinity equations (including advective terms) and on the optimization of adjustable coefficients with a genetic algorithm. Adjusted fluxes allow us to simulate the average sea surface temperature and salinity with errors less than 0.02°C and 0.02 psu, respectively, over 1 year. The corresponding new surface heat budget indicates that the adjusted annual net heat (+17 W m^{-2}) is weaker than previously calculated (+33 W m^{-2}) but remains positive, meaning a heat gain for the ocean. The adjusted annual salt budget reveals a net evaporation of 0.75 mm d^{-1} for the POMME region. In contrast with climatology we find that the zone is located southward of the null buoyancy flux area during September 2000–September 2001.

Citation: Caniaux, G., S. Belamari, H. Giordani, A. Paci, L. Prieur, and G. Reverdin (2005), A 1 year sea surface heat budget in the northeastern Atlantic basin during the POMME experiment: 2. Flux optimization, *J. Geophys. Res.*, *110*, C07S03, doi:10.1029/2004JC002695.

1. Introduction

[2] The problem of heat and salt budget closure is an important subject in operational and research oceanography due to biases in bulk formula estimates and the spatial/temporal resolution of input data used for estimating fluxes. Inconsistent fluxes result in a misleading thermal and salt content of the upper ocean, leading to forced (or coupled) oceanic models to diverge. Generally, flux corrections are systematically applied in order to avoid large drifts of the models [*Barnier et al.*, 1995]. Sea surface temperature in turn affects air-sea exchanges and it is difficult to determine the part of the model errors due to uncertainties in the knowledge of surface forcing and that related to errors in the (thermo)dynamics of the model [*Barnier*, 1999].

0148-0227/05/2004JC002695

[3] This problem was examined at climatological scales by *Isemer et al.* [1989] and *Macdonald and Wunsch* [1996], by using inverse methods and ocean heat transport constraints. *Josey et al.* [1999] estimated corrections of the Southampton Oceanography Center (SOC) air-sea flux climatology and concluded that the closure of the ocean heat budget was not obtained, as the global mean net heat flux is an oceanic gain of 30 W m^{-2}. With an inverse approach, *Grist and Josey* [2003] computed adjusted climatological fluxes and proposed flux corrections to the SOC climatology that led to improvements relative to the preceding study. They also noted that further constraints on oceanic transport were required at small temporal and spatial scales to compare their climatology to in situ data.

[4] *Trenberth* [1997] used another technique whereby adjusted global fluxes were estimated by using atmospheric budgets as a constraint and found that gross violations of

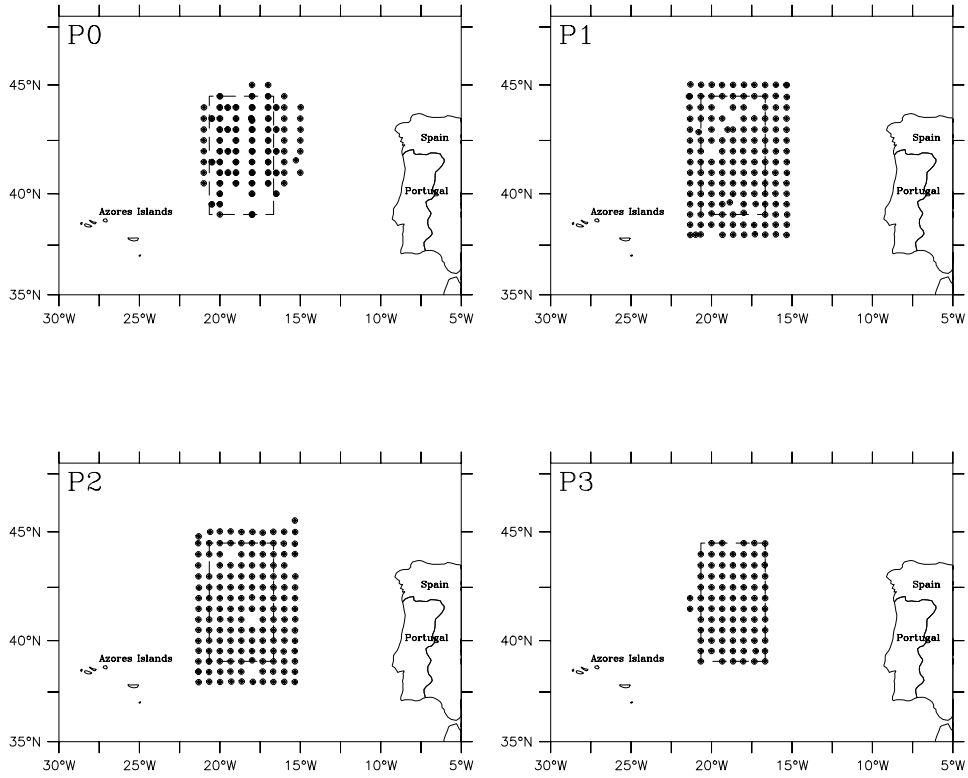

Figure 1. Maps of the four hydrographic networks performed during Programme Océan Multidisciplinaire Méso Echelle (POMME) with the position of the conductivity-temperature-depth (CTD) casts (dots). Dashed lines correspond to the widest domain common to all networks.

the mass budget are present in the NCEP reanalyses, even with a four-dimensional data assimilation system. *Curry et al.* [1999] used atmospheric temperature and humidity (Q1 and Q2) budgets to estimate the accuracy of TOGA/COARE sea surface fluxes. These authors concluded that the heat budget over the TOGA/COARE area could not be regarded as closed to better than about 20%, with an imbalance in the heat budget of 34 W m^{-2}, which is the order of magnitude of the net heat flux. Fluxes were also inferred from differences between oceanic heat content change and estimates of advection and diffusion by *Behringer and Stommel* [1981] in the tropical Atlantic. *McCulloch and Leach* [1998] inferred air-sea fluxes from an upper ocean heat budget northeast of the Azores and concluded that in this region and with this approach it was possible to constrain the heat flux, with an error of only to 25 W m^{-2} due to weak advection and diffusion.

[5] In this context, a specific study was carried out by *Caniaux et al.* [2005] to estimate air-sea fluxes in the northeast Atlantic over a 1 year period (September 2000–October 2001) as part of the Programme Océan Multidisciplinaire Méso Echelle (POMME). One of the main objectives of this experiment was to specify the role of oceanic mesoscale processes on the 11°–13°C water subduction in the Northeast Atlantic [*Mémery et al.*, 2005]. This complicated process was investigated by four Intensive Observation Periods (IOP), called POMME0 (hereafter P0, September–October 2000), POMME1 (P1, February–March 2001), POMME2 (P2, March–May 2001) and POMME3 (P3, September–October 2001). Figure 1 portrays the area where measurements were made (21°–15°W, 38°–45°N) and the location of the conductivity-temperature-depth (CTD) casts performed during each hydrographic network. More details of the experimental strategy can be found in *Mémery et al.* [2005] and *Reverdin et al.* [2005].

[6] The approach used by *Caniaux et al.* [2005] to compute the heat and freshwater budgets for this region consisted in selecting the best available products to estimate each component of the heat, salt and momentum fluxes (hereafter referred to as PFE, for POMME Flux Estimates) as in *Caniaux and Planton* [1998]. Hourly surface irradiances (solar and downward longwave radiative fluxes) were derived from the geostationary Meteosat satellite data set collected at the Centre de Météorologie Spatiale (Meteo-France, Lannion) following the method developed by *Brisson et al.* [1994]. Daily sea surface temperature (SST) analyses were produced from satellite (NOAA) and in situ data (more than 150 000 SSTs collected during the experiment). Atmospheric parameters (pressure, temperature, wind, humidity, and precipitation) were issued from the European Center for Medium Range Weather Forecasts (ECMWF) model and a state-of-the-art algorithm was used to compute turbulent fluxes at a 5 km resolution. Model atmospheric parameters and deduced fluxes were validated against measurements issued from a moored buoy and from the R/V *L'Atalante*.

[7] The mean annual heat budget determined by this approach indicates an ocean heat gain of +33 W m^{-2} (a positive flux indicates a heat gain for the ocean and a negative flux a heat loss). By comparison, the ECMWF

model and the French operational numerical weather prediction ARPEGE model [*Courtier et al.*, 1991] produce a negative annual budget for this region of -9 W m^{-2} and -25 W m^{-2} respectively, corresponding to a net cooling of the ocean. Recent results by *Moyer and Weller* [1997] and *Weller et al.* [2004], using measurements collected over 2 years (1991–1993) at the northeast mooring of the Subduction Experiment (located south of the POMME area) indicate a positive (around +15 W m^{-2}) though weaker mean net heat budget relative to our PFE.

[8] The question addressed in this paper is the validation of these different flux estimates by considering the heat and freshwater budget closure. The method proposed here is to test the accuracy of the PFE through the use of a numerical model, and to find which correction should be applied to the fluxes so that the equations of heat and salt in the mixed layer can be balanced. This implies to perform numerous sensitivity tests, not only for the surface fluxes but also for the parameterizations used in the model. It is therefore not possible to use a three dimensional model, for obvious computer time reasons. We have instead applied a one-dimensional (1-D) model in order to simulate the whole POMME area. Such an approach can be used because the POMME area is located in the intergyre region of the northeast Atlantic, with weak eddy kinetic energy and mesoscale activity compared to most midlatitude areas [*Ducet et al.*, 2000] and a weak impact of the large-scale flow on the temperature and salinity advection compared to surface forcing [*Caniaux and Planton*, 1998].

[9] The paper is organized as follows. Section 2 provides a description of the 1-D approach including the set of equations to be solved and the way to estimate the forcing terms. The optimization method is described in section 3: the 1-D simulation is optimized with a genetic algorithm that searches for the best set of selected parameters (flux corrections among them) to realistically reproduce the observations collected during the experiment. Results including the new heat, salt and buoyancy budgets are presented in section 4. Conclusions are drawn in section 5.

2. One-Dimensional Approach

[10] This approach requires (1) solving an adequate set of equations fitted to describe a whole geographical area; (2) estimating the terms of the equations that cannot be solved explicitly; and (3) checking a posteriori the assumptions made by using more sophisticated models. This last point is considered to be outside of the scope of the present paper.

2.1. Equations

[11] In this section, the equation of temperature is modified in order to simulate with a 1-D mixed layer model the evolution of a mean temperature profile (i.e., representing the whole POMME domain). The evolution of temperature T is described by the following equation [*Holton*, 1992]:

$$\partial_t T = \frac{F_{\mathrm{sol}}}{\rho_0 C_p}\partial_z I(z) - \partial_z \overline{T'w'} - \mathbf{U}.\nabla_h T - w\partial_z T - \nabla\left(\overline{T'.\mathbf{U}'}\right), \quad (1)$$

where the temperature tendency results from net solar radiation input (F_{sol}), vertical turbulent mixing, horizontal and vertical advection and horizontal diffusion. ρ_0 and C_p are the density and specific heat capacity of sea water and $I(z)$ is the fraction of the net solar radiation that penetrates to depth z. Here the single prime refers to the small unresolved turbulent scales involved. Using a classical K profile parameterization for the vertical mixing, the evolution of temperature is

$$\partial_t T = \frac{F_{\mathrm{sol}}}{\rho_0 C_p}\partial_z I(z) + \partial_z(K\partial_z T) - \mathbf{U}.\nabla_h T - w\partial_z T - \nabla\left(\overline{T'.\mathbf{U}'}\right). \quad (2)$$

[12] In order to represent the spatial mean over the whole POMME area, a space averaging operator (denoted with angle brackets) is introduced and applied to equation (2):

$$\partial_t\langle T\rangle = \frac{\langle F_{\mathrm{sol}}\partial_z I(z)\rangle}{\rho_0 C_p} + \partial_z\langle K\partial_z T\rangle - \langle \mathbf{U}.\nabla_h T\rangle - \langle w\partial_z T\rangle - \left\langle \nabla\left(\overline{T'.\mathbf{U}'}\right)\right\rangle. \quad (3)$$

As the Ekman transport can be computed from the PFE, the current is split into an Ekman contribution (subscript e) and the residual (noted "non-Ekman," subscript ne):

$$\mathbf{U} = \mathbf{U_e} + \mathbf{U_{ne}} \quad (4)$$

$$w = w_e + w_{ne}. \quad (5)$$

Applied to equation (3), this leads to

$$\partial_t\langle T\rangle = \frac{\langle F_{\mathrm{sol}}\partial_z I(z)\rangle}{\rho_0 C_p} + \partial_z\langle K\partial_z T\rangle - \langle \mathbf{U_e}.\nabla_h T\rangle - \langle \mathbf{U_{ne}}.\nabla_h T\rangle - \langle w_e\partial_z T\rangle - \langle w_{ne}\partial_z T\rangle - \left\langle \nabla\left(\overline{T'.\mathbf{U}'}\right)\right\rangle. \quad (6)$$

[13] A decomposition into spatial mean and deviation from this mean (noted with a double prime) is performed for the solar penetration, turbulent vertical mixing, and vertical Ekman advection nonlinear terms:

$$\langle F_{\mathrm{sol}}\partial_z I(z)\rangle = \langle F_{\mathrm{sol}}\rangle\partial_z\langle I(z)\rangle + \left\langle F''_{\mathrm{sol}}\partial_z I(z)''\right\rangle, \quad (7)$$

$$\partial_z\langle K\partial_z T\rangle = \partial_z\langle K\rangle\partial_z\langle T\rangle + \partial_z\langle K''\partial_z T''\rangle, \quad (8)$$

$$\langle w_e\partial_z T\rangle = \langle w_e\rangle\partial_z\langle T\rangle + \left\langle w''_e\partial_z T''\right\rangle. \quad (9)$$

Equation (6) is then rewritten as

$$\partial_t\langle T\rangle = \frac{\langle F_{\mathrm{sol}}\rangle}{\rho_0 C_p}\partial_z\langle I(z)\rangle + \partial_z\langle K\rangle\partial_z\langle T\rangle - \langle \mathbf{U_e}.\nabla_h T\rangle - \langle w_e\rangle\partial_z\langle T\rangle + \partial_z\langle K''\partial_z T''\rangle - [\langle \mathbf{U_{ne}}.\nabla_h T\rangle + \langle w_{ne}\partial_z T\rangle] + \frac{\left\langle F''_{\mathrm{sol}}\partial_z I(z)''\right\rangle}{\rho_0 C_p} - \left\langle w''_e\partial_z T''\right\rangle - \left\langle \nabla\left(\overline{T'.\mathbf{U}'}\right)\right\rangle. \quad (10)$$

[14] A similar equation can be obtained for the mean salinity $\langle S\rangle$, except that the surface forcing is evaporation minus precipitation. Solving equation (10) requires the ability to evaluate all the terms in brackets. Some of them are computed at each time step by the numerical 1-D model

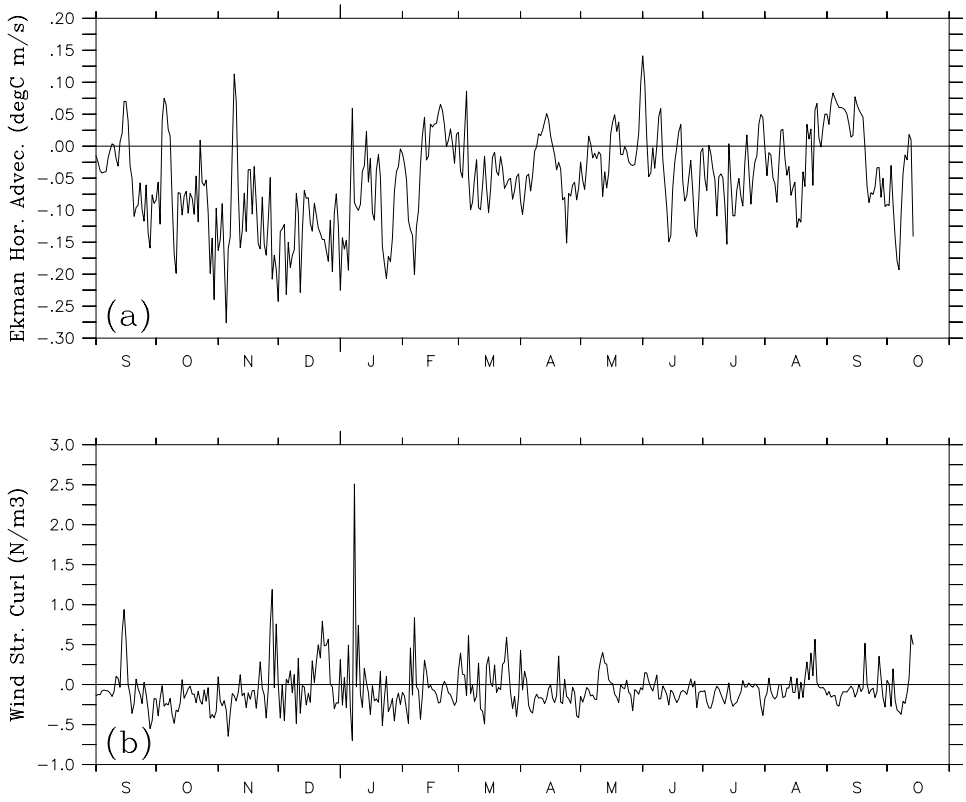

Figure 2. Temporal evolution of the domain average: (a) horizontal Ekman advection of temperature integrated over the Ekman layer depth (ELD) in °C m s^{-1} and (b) wind stress curl in N m^{-3}.

(for instance $\partial_z \langle T \rangle$ and $\langle K \rangle$). Others are evaluated using the PFE averaged over the POMME area: for instance, the mean solar penetration is directly obtained using the spatially averaged shortwave flux, while the Ekman transport terms are evaluated from the wind stress spatial mean as described in section 2.2. The other advective terms (called ''non-Ekman'') are estimated from the evolution of the observed mean temperature and salinity profiles (section 2.3.). The subgrid-scale terms (nonlinear contributions corresponding to the deviation from the spatial mean and noted with double prime) need to be estimated (section 2.4.). Lastly, the horizontal tracer diffusion $-\langle \nabla(\overline{T'.\mathbf{U}'}) \rangle$ due to small turbulent scales, which is small even in regions of strong horizontal gradient, is assumed to remain negligible when spatially averaged.

2.2. Ekman Transport

2.2.1. Horizontal Ekman Advection

[15] The response of the upper layer oceanic circulation to wind forcing can be obtained from the Ekman transport theory. The horizontal Ekman advection of temperature ($-\langle \mathbf{U_e}.\nabla_h T \rangle$ in equation (10)) is estimated under the assumption that, inside the Ekman layer, the temperature is vertically homogeneous enough to be assimilated to the SST. This hypothesis is legitimate, as the Ekman layer depth (ELD) is almost always shallower than the MLD [*Cushman-Roisin*, 1987]. The horizontal Ekman advection can then be estimated as

$$-\langle \mathbf{U_e}.\nabla_h T \rangle \approx -\langle \mathbf{U_e}.\nabla_h \mathrm{SST} \rangle = -\left\langle \frac{\mathbf{k} \wedge \boldsymbol{\tau}}{\rho_0 f h_e}.\nabla_h \mathrm{SST} \right\rangle, \quad (11)$$

where $\mathbf{k}$ is the vertical unit vector, $\boldsymbol{\tau}$ the wind stress, f the Coriolis parameter and h_e the ELD, calculated following *Cushman-Roisin* [1987]:

$$h_e = 0.4 \frac{u_*}{f}, \quad (12)$$

where u_* is the turbulent friction velocity defined from the magnitude of the stress (τ) along the boundary by

$$u_* = \sqrt{\frac{\tau}{\rho_0}}. \quad (13)$$

[16] The evolution of the spatially averaged horizontal Ekman advection integrated over the ELD is reproduced in Figure 2a. The annual mean is negative (-0.052×10^{-6} °C m s^{-1}), in agreement with the north to south Ekman transport and the mean north to south SST gradient: it thus induces an annual mean cooling for the top layers. Figure 2a clearly indicates that this cooling is particularly intense from October to January with peak values in December, i.e., when the wind stress reaches its highest values.

[17] The horizontal Ekman advection of salinity was estimated using the same procedure. Sea surface salinity (SSS) analyses were performed over the whole Atlantic basin by G. Reverdin et al. (In situ surface salinity in the tropical and subtropical Atlantic Ocean, part 1, Large scale variability, submitted to *Progress in Oceanography*, 2005), using thermosalinograph data. The analyses produced by these authors have a much coarser temporal (1 month) and

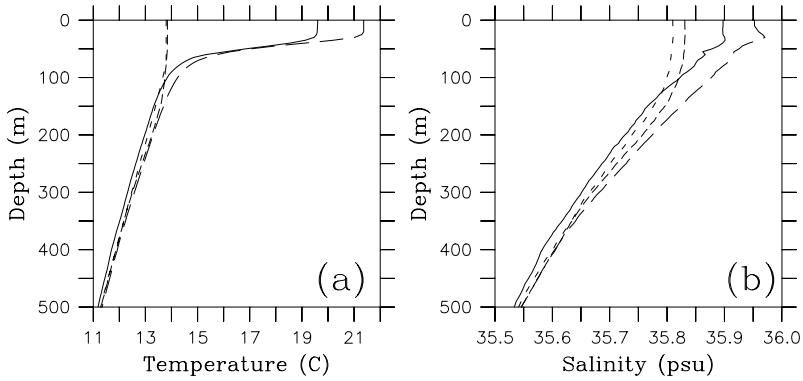

Figure 3. Mean (a) temperature and (b) salinity profiles issued from the CTD measurements made during P0 (solid line), P1 (small dashed line), P2 (dashed line), and P3 (long dashed line).

spatial (1° longitude × 1° latitude) resolution than the PFE SST analyses, due to the rather sparse sampling of the in situ data. Inconsistencies may result from the different resolution of temperature and salinity analyses, specially with the Ekman advection, and may affect the vertical mixing in the mixed layer. This is the reason why less weight will be attributed to salinity in the cost function used to optimize the model (see section 3.3). SSS fields were bilinearly interpolated onto a regular 5 km grid over the POMME domain, and then linearly interpolated to 1 day sampling, before being combined with the wind stress to get the horizontal Ekman advection. Despite the resolution, an evolution very similar to Figure 2a was obtained for the salinity (not shown).

2.2.2. Vertical Ekman Advection

[18] The spatially averaged vertical Ekman velocity $\langle w_e \rangle$ is calculated from the wind stress curl [*Gill*, 1982]:

$$\langle w_e \rangle = \left\langle \frac{1}{\rho_0 f} (\nabla \wedge \tau)\mathbf{k} \right\rangle. \quad (14)$$

In the 1-D model, a profile of $\langle w_e \rangle$ is needed and reconstructed as follows: zero at the surface, maximum at the base of the ELD, and then reduced linearly towards zero at the bottom. The vertical Ekman advection of temperature ($-\langle w_e \rangle\ \partial_z\ \langle T \rangle$ in equation (10)) is then calculated from the model temperature profile ($\partial_z \langle T \rangle$).

[19] Figure 2b displays the temporal evolution of the mean wind stress curl. It gives insights into the evolution of the spatially averaged vertical Ekman velocity, as these two fields are proportional. An anticyclonic circulation prevailed throughout the year (annual mean: -0.057×10^{-6} N m^{-3}), inducing a mean downward vertical velocity of 18 m yr^{-1} into the ocean, in agreement with climatological values of *Marshall et al.* [1993] and *Qiu and Huang* [1995]. In contrast, short time periods are associated with positive values of the wind stress curl. These positive peaks, mainly observed from December 2000 to March 2001, were associated with the passage of atmospheric extratropical cyclones through the area, consistent with the meteorological conditions observed over the POMME region.

2.3. Non-Ekman Advection

[20] The evolution of the spatially averaged temperature and salinity profiles is characterized by a shift between P0 and P1, P1 and P2, and P2 and P3 below 300 m (Figure 3). Such an evolution, at a greater depth than the spatially averaged MLD, can mainly be attributed to advective processes. We have thus assumed that the shifts observed below 300 m between the profiles were due to the horizontal and vertical non-Ekman advections. As a result, the corresponding term in equation (10) ($-[\langle \mathbf{U_{ne}}.\nabla_h T \rangle + \langle w_{ne} \partial_z T \rangle]$) was derived from the mean evolution observed below 300 m between P0 and P1, P1 and P2, P2 and P3, and introduced in the 1-D model as another forcing. The corresponding temperature and salinity tendency was thus added at each time step and each level to the temperature and salinity equations, under the assumption that this evolution was constant between two hydrographic surveys.

2.4. Subgrid-Scale Processes

2.4.1. Subgrid-Scale Vertical Mixing

[21] The subgrid-scale vertical mixing ($\partial_z \langle K'' \partial_z T'' \rangle$ in equation (10)) is difficult to estimate and is poorly documented in the literature. Tests indicate that this term is important and that the corrected fluxes become unrealistic without it. We have assumed that this term tends to increase the vertical mixing simulated by the 1-D model. We have also assumed that this additional contribution to vertical mixing is induced by the subgrid-scale fluctuations of the wind field throughout the domain considered. Consequently, the subgrid-scale vertical mixing contribution was taken into account by increasing the wind stress by a factor of $\alpha = (1 + \sigma)/(\langle U \rangle)^2$ where σ denotes the root mean square (rms) of the wind velocity U. As time series of daily values of α have demonstrated that this coefficient is more or less constant throughout the year (not shown), the wind stress was multiplied by the constant value $\alpha = 1.4$.

2.4.2. Subgrid-Scale Solar Penetration and Vertical Ekman Advection

[22] The two other subgrid-scale contributions were assumed to be negligible. The subgrid-scale term due to solar penetration ($(\langle F''_{sol} \partial_z I(z)'' \rangle)/(\rho_0 C_p)$ in equation (10)) can be neglected as there was no observational evidence for a strong spatial correlation between irradiance and the solar penetration law (which depends on pigments) during the POMME surveys (H. Claustre, personal communication). Note that this hypothesis is largely used in modeling studies. The subgrid-scale vertical Ekman advection $\langle w''_e \partial_z T'' \rangle$ is assumed to be some orders of magnitude lower

than the contribution of the mean vertical Ekman current (term $\langle w_e \rangle \partial_z \langle T \rangle$ in equation (10)); it is therefore neglected.

2.5. Numerical Aspects

[23] The basic 1-D model used to solve equation (10) and its equivalent for salinity is the *Gaspar et al.* [1990] model of vertical mixing. This model solves the heat, salt and momentum equations with a 1.5 turbulent closure based on a turbulent kinetic energy equation. The initial version of this model was improved by introducing a new parameterization of the diapycnal mixing [*Large et al.*, 1994] in order to better reproduce the nonlocal source of vertical mixing in the stratified water column below the boundary layer. The model was also amended to take into account the advective terms of equation (10). The vertical Ekman advection terms for tracers are calculated with an upstream numerical scheme, while all other advective terms are considered as external forcings, i.e., added at each time step to the tracer equations. Moreover, horizontal Ekman advection is added to the tracer equations at each level inside the Ekman layer. The vertical resolution of the model is regular and equal to 5 m from the surface down to the 500 m deep bottom level. The surface forcings, the vertical Ekman velocity and the horizontal Ekman advection terms are computed every day from the PFE, then averaged over the whole domain and finally linearly interpolated at each model time step (10 min).

[24] The model is initialized with the average of the 54 CTD profiles collected during P0 over the area limited to longitudes 20.66°–16.66°W and to latitudes 39.00°–44.50°N (Figure 1). This region corresponds to the widest area (roughly 330 km × 670 km) common to P0, P1, P2 and P3. As the sampling strategy was almost identical during the networks, the heat and salt budget estimates can be considered as homogeneous. To test this hypothesis, a bootstrap technique was implemented, consisting in evaluating the standard deviation (std) of the temperature and salinity spatial mean profiles when changing randomly one CTD by another one, and when repeating the substitution N times. This led to the conclusion that in the top 500 m layers, the value of the bootstrap std at each level was less than 0.02°C for temperature. This corresponds to a heat content of 4×10^7 J m^{-2}, or equivalently to an accuracy of 1 W m^{-2} for the period P0–P3. The conclusion is that the CTD sampling leads to an accuracy in the flux correction of 1 W m^{-2}, which is quite satisfactory.

3. Optimization

[25] The optimization of the 1-D simulation requires the optimization of both the 1-D model and the surface forcings (precipitation and turbulent fluxes). Therefore adjustable parameters need to be selected either to tune poorly known constants of the 1-D model or to correct the turbulent fluxes, keeping in mind that the efficiency of the optimization technique depends strongly on the number of parameters to be optimized. Finally, a set of eight parameters was chosen: three for the model optimization and five for the flux correction.

3.1. Model Optimization

[26] As previously mentioned, some of the constants used in the physical parameterizations of the 1-D model are poorly known. However they play an important role in the results of the simulations and have to be determined in an optimal way. These adjustable constants were selected after many sensitivity tests were performed with the model.

3.1.1. Solar Radiation (One Parameter)

[27] The parameterization used in the 1-D model relies on the classical double exponential transmission profile proposed by *Paulson and Simpson* [1977]:

$$I(z) = R \exp\frac{-z}{D_1} + (1-R)\exp\frac{-z}{D_2},$$

where z is the depth, and R is a partition parameter between the red part of the radiation spectrum penetrating down to the extinction depth D_1 and the blue-green part penetrating down to the extinction depth D_2. Generally, red light has a rapid attenuation in the upper few meters compared to blue-green light [*Paulson and Simpson*, 1977]. Sensitivity tests proved that SST is very sensitive to D_2 and R but not to D_1. Despite its high sensitivity, the parameter R that gives the red fraction of the radiation penetrating into the ocean is to be fixed as a physical constraint [*Jerlov*, 1974; *Prieur and Legendre*, 1988]. We thus decided to solely retain D_2 as an adjustable parameter and to fix R and D_1 to values corresponding to waters ranging from IB to III according to the *Jerlov* [1976] classification ($R = 0.74$ and $D_1 = 1.3$ m), consistently with *Simonot and Le Treut* [1986] values for the POMME area.

3.1.2. Diapycnal Mixing (Two Parameters)

[28] In the model, the vertical mixing below the MLD is written as the superposition of turbulent mixing induced by vertical shear instability and by internal wave breaking [*Large et al.*, 1994]. Diffusivity due to internal wave breaking is parameterized by a constant, which differs between tracers (ϵ) and momentum (ω). The value of these constants is not well defined in the literature. For instance, *Kantha and Clayson* [1994] suggest that $\epsilon = 5 \times 10^{-5}$ m^2 s^{-1}, while *Ledwell et al.* [1993] and *Large et al.* [1994] propose much smaller values (1.1×10^{-5} m^2 s^{-1} and 1×10^{-5} m^2 s^{-1}, respectively). According to *Peters et al.* [1988], the magnitude of internal wave momentum viscosity ω should be 7 to 10 times larger than that of scalar diffusivity, so that *Large et al.* [1994] adopt a constant value of 1×10^{-4} m^2 s^{-1}. Sensitivity tests proved that the results of the simulations were very dependent on the value of ϵ, especially during the period of spring stratification, and in a minor way on that of ω. These two constants were thus judged to be optimized.

3.2. Turbulent Flux Optimization

[29] As stated by *Caniaux et al.* [2005], the satellite radiative fluxes of the PFE compare very well with independent in situ measurements. We have thus decided to use these gridded radiative fluxes as they stand, considering that no correction is justified for them. On the other hand, turbulent fluxes and precipitation are generally subject to errors due to uncertainties in both the bulk formulae and the meteo-oceanic parameters [*Blanc*, 1985; *Eymard et al.*, 1999]; they therefore need to be corrected.

[30] Several possibilities arise as errors in these fluxes may be attributed either to the transfer coefficients used in the bulk formulae, or to the original air-sea parameters, or to both of them [*WGASF Group*, 2000]. Moreover, errors in

Table 1. List of Adjustable Parameters, With Their Range of Values and the Optimum Obtained With the Genetic Algorithm

Parameter	Range of Value	Optimum
D_2, m	5–30	20.0
ϵ, $m^2\ s^{-1}$	1×10^{-5}–8×10^{-5}	6.4×10^{-5}
ω, $m^2\ s^{-1}$	0.7×10^{-4}–3×10^{-4}	0.88×10^{-4}
β_{st}	0.9–1.1	0.967
β_s	−2–10	7.994
β_l	0.6–1.4	0.988
β_w	1–1.2	1.134
β_p	0.4–0.9	0.545

the wind are likely to simultaneously affect the wind stress, latent and sensible heat. Finally, we decided to correct the original turbulent fluxes (wind stress $\tau^* = \rho_a C_d U^2$; latent heat $Q^*_{\text{lat}} = \rho_a C_p C_e (q_s - q_a) U$ and sensible heat $Q^*_{\text{sen}} = \rho_a L_v (\text{SST} - T_a) U$) by introducing four adjustable coefficients (β_{st}, β_w, β_s and β_l) as follows:

$$\tau = \rho_a [\beta_{st} C_d][\beta_w U]^2 = \beta_{st}\beta_w^2 \tau^*, \tag{15}$$

$$Q_{\text{lat}} = \rho_a C_p [\beta_l C_e (q_s - q_a)][\beta_w U] = \beta_l \beta_w Q^*_{\text{lat}}, \tag{16}$$

$$Q_{\text{sen}} = \rho_a L_v C_h (\text{SST} - T_a)[\beta_w U] - \beta_s = \beta_w Q^*_{\text{sen}} - \beta_s. \tag{17}$$

In these expressions, ρ_a stands for the air density, L_v the latent specific heat, C_p the specific heat capacity; q_s is the surface specific humidity, U the wind velocity, T_a and q_a the air temperature and the air specific humidity, and C_d, C_e, C_h are the transfer coefficients. β_w, which appears in the formulation of all the turbulent fluxes, is assumed to correct the errors affecting the wind. β_{st} is introduced in the wind stress formulation to correct the errors due to the transfer coefficient C_d. β_l is introduced to correct both the errors due to the transfer coefficient C_e and to the difference between the sea surface and the air specific humidity. Evaporation (which is part of the water budget E-P) is then adjusted using the same multiplying coefficients ($\beta_l\beta_w$) as the latent heat. In contrast to the other turbulent fluxes which are solely corrected through multiplying coefficients, a bias β_s is introduced in the sensible heat flux formulation, as this flux may vary from negative to positive values.

[31] Precipitation is also an important factor for the salinity tendency, which affects density and vertical mixing. *Caniaux et al.* [2005] indicated that the E-P budget of the PFE was not very reliable for two reasons: (1) its accuracy could not be evaluated from comparison with in situ measurements and (2) precipitation rates of the ECMWF model are largely uncertain. They indeed can reach values 10% to 30% higher than climatologies in the extra-tropics with a tendency of a balance between precipitation and evaporation [*Arpe and Roeckner*, 1999; *Beranger et al.*, 1999]. To take this into account, the original precipitation (P^*) was adjusted through the introduction of a multiplying coefficient β_p:

$$P = \beta_p P^*. \tag{18}$$

The ranges in the value of the eight adjustable parameters (Table 1) were selected to be large enough to be sure to get the optimum but in reasonable intervals to discard unphysical solutions. Note that the wind stress correction ($\beta_{st}\beta_w^2$) was also applied to the Ekman transport terms, because of their obvious dependence on the wind stress.

3.3. Genetic Algorithm

[32] The optimization of the 1-D simulations was carried out using a genetic algorithm (GA) [*Carroll*, 1996]. GAs are based on techniques derived from genetics and population evolution. The method, developed from the concepts of *Holland* [1975], aims to efficiently seek the extrema of complex functions. Compared to traditional optimization methods based on the gradient of a function, a GA is more appropriate when the function has several extrema, or is discontinuous [*Barth*, 1992]. The algorithm searches in a N dimensional space the N parameters that minimize a cost function evaluated for each run of the model. As output, a set of N optimal parameters is obtained.

[33] GAs first code the set of parameters to be optimized in a binary form called chromosome. The algorithm then starts with a randomly chosen population of chromosomes. The second step is to evaluate the fitness value of each chromosome by computing a cost function, using the corresponding set of parameters to run the model. Then, the three genetic processes of (1) selection, (2) crossover, and (3) mutation are performed upon the chromosomes in sequence. During the selection, chromosomes are copied in proportion to their fitness values based on a probability of selection (defined as the fitness value of a particular chromosome divided by the sum of the fitness values of all chromosomes). Crossover then acts on the selected chromosomes, using a crossover probability: this operator selects a crossover site within paired strings and exchanges between the two chromosomes the parts located to the right of the crossover site. Lastly, mutation, which involves changing a part at random based on mutation probability, is applied to the chromosomes in order to maintain diversity. After the execution of these three processes, the new chromosomes are compared to the previous generation, and accepted (or rejected) based on an update probability. The procedure is then repeated until convergence is reached (i.e., when the fitness of all the chromosomes becomes very close to one another), or stopped by fixing a maximum number of generations.

[34] In the present study a set of $N = 8$ parameters is to be determined. The cost function is based on the difference between observed and simulated SST and SSS, and temperature and salinity vertical profiles. Observed SST and SSS are deduced from daily analyses averaged over the inner POMME domain (Figure 1), while the observed temperature and salinity profiles are deduced from the P1, P2, and P3 CTD networks. The exact formulation of the cost function (CF) is as follows:

$$\begin{aligned}\text{CF} = {} & \alpha_1 \sum_i \left(\frac{1}{\sigma^2_{\text{SST}}}\right)(\text{SST}_{\text{model}} - \text{SST}_{\text{obs}})^2 \\ & + \alpha_2 \sum_i \left(\frac{1}{\sigma^2_{\text{SSS}}}\right)(\text{SSS}_{\text{model}} - \text{SSS}_{\text{obs}})^2 \\ & + \alpha_3 \sum_{\text{P1,P2,P3}} \left(\frac{1}{\sigma^2_{T(z)}}\right) \sum_{k=1}^{K} (T_{\text{model}}(k) - T_{\text{obs}}(k))^2 \\ & + \alpha_4 \sum_{\text{P1,P2,P3}} \left(\frac{1}{\sigma^2_{S(z)}}\right) \sum_{k=1}^{K} (S_{\text{model}}(k) - S_{\text{obs}}(k))^2. \end{aligned} \tag{19}$$

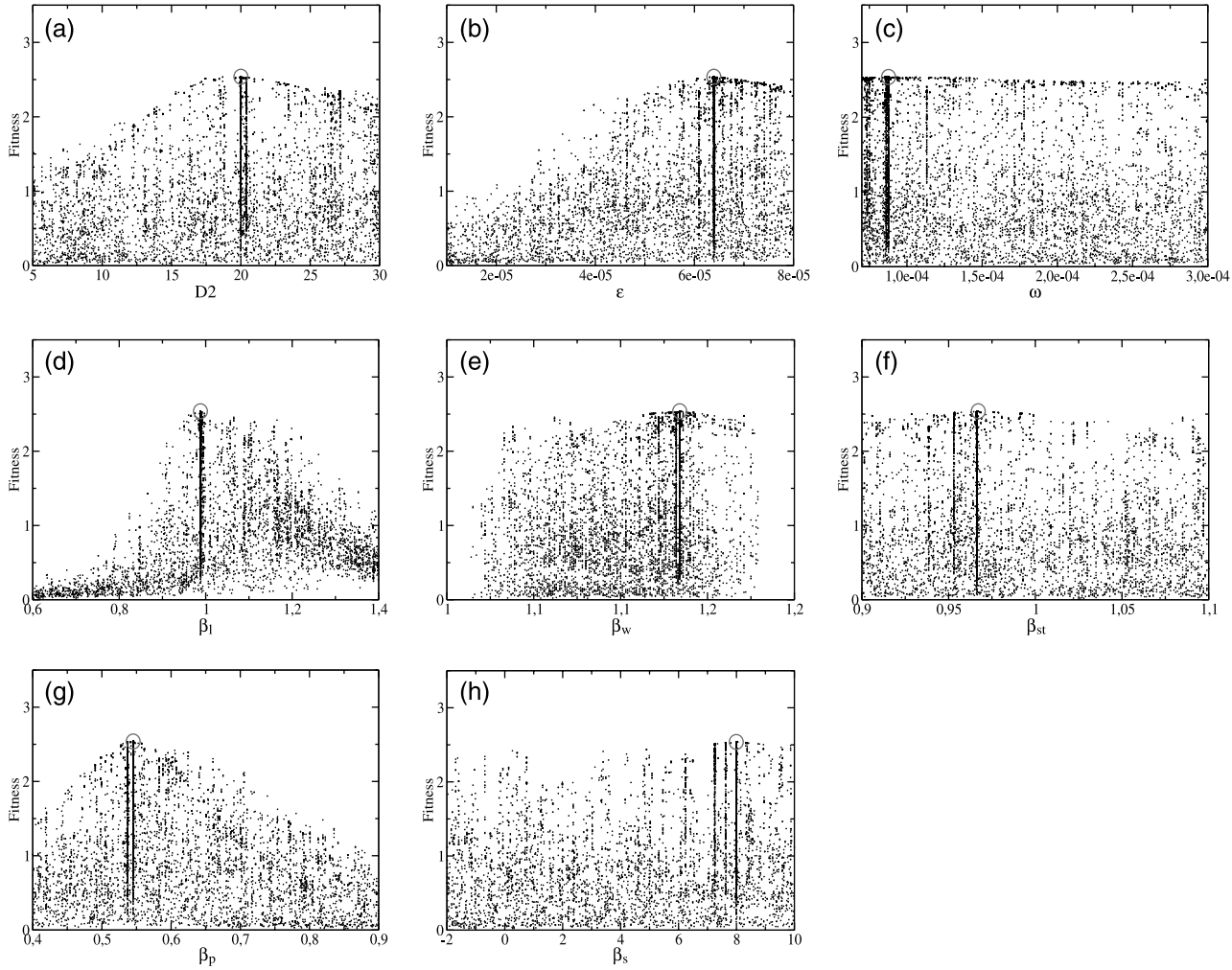

Figure 4. Fitness function obtained for each adjustable parameter: (a) D_2; (b) ϵ; (c) ω; (d) β_l; (e) β_w; (f) β_{st}; (g) β_p; and (h) β_s. The maximum fitness is circled.

The difference between model and data is cumulative over the whole period of simulation (index i), and over the K = 40 uppermost levels (to a depth of 200 m) of the temperature and salinity profiles (index k). Each contribution is normalized by the corresponding variance of the data (noted σ^2). Lastly, the various contributions are weighted through the coefficients α_1, α_2, α_3, α_4 taken as equal to 1, 1×10^{-1}, 3, and 3×10^{-1}, respectively, to confer to each term of the cost function a weight inversely proportional to the number of data. Note that this cost function attributes less weight to the salinity than to the temperature, consistently with the lower confidence we have in the SSS analyses and forcing data. The efficiency of the optimization is then evaluated through a parameter called fitness, which is inversely proportional to the cost function (Fitness = 100/CF).

4. Results

4.1. Adjusted Parameters

[35] The optimization algorithm allowed us to run some 10000 1-year-long simulations covering the POMME experiment duration. For each simulation, the eight adjustable parameters are chosen by the GA in their preselected range of values, and the cost function is computed. The corresponding fitness is plotted in Figures 4a–4h, as a function of the adjustable parameters. Each dot represents the value of the fitness obtained for one simulation performed with one set of adjustable parameters. The optimal value of the adjustable parameters is given where the fitness reaches its maximum. Note that in each plot of Figure 4 the envelope of the points highlights the sensitivity of the optimization while the lines near the optimum indicate the way the GA works. These lines correspond to sequences where the GA tests several sets of parameters while keeping the optimal value obtained for one specific parameter. Each line is in fact formed by the proximity of points corresponding to different values of the fitness function obtained with a fixed parameter, the other seven ones varying inside their respective range of values.

[36] The optimum obtained for the solar penetration parameter (D_2 = 20 m) is somewhat higher than those in the *Jerlov* [1976] classification (in the range of 17 m to 7.9 m for Water Type IB, II and III). This value is however quite relevant, as it does not correspond to a particular type of water, but is supposed to represent the annual average of different types of water which may vary throughout the year from clear to less transparent (for

Table 2. Comparison of Adjusted and Unadjusted Mean Annual Budgets, Averaged Over the Domain (21.33°–15.33°W, 38°–45°N)[a]

Flux	Adjusted	Unadjusted	Difference
Latent	−74.7	−66.7	−8.0
Sensible	−8.2	−0.2	−8.0
Net heat	17.0	33.0	−16.0
Wind stress	0.138	0.111	0.027
E-P	0.75	−1.10	1.85
P	1.9	3.4	−1.5

[a]Heat fluxes are in W m^{-2}; wind stress is in N m^{-2}; *E-P* and *P* are in mm d^{-1}. Period considered is 2 September 2000–2001.

instance, when the bloom occurs). The adjusted scalar diffusivity due to internal waves activity in the pycnocline ($\epsilon = 6.4 \times 10^{-5}$ m^2 s^{-1}) is close to that proposed by *Kantha and Clayson* [1994] (5×10^{-5} m^2 s^{-1}). The optimal value of the internal wave momentum viscosity ($\omega = 0.88 \times 10^{-4}$ m^2 s^{-1}) is also consistent with the results of these authors (1×10^{-4} m^2 s^{-1}) but does not correspond to any neat peak of the fitness (Figure 4c), confirming the weak sensitivity of the simulations to this parameter.

[37] In Figure 4, quite neat peaks are obtained for all the other adjustable parameters, in particular for the latent heat (β_l), wind (β_w) and precipitation (β_p) (Figures 4d, 4e, and 4g, respectively). This indicates that, inside the range of values of the adjustable parameters, the solution is unique. This result provides confidence in the corrections to be applied to the fluxes.

[38] The combined use of these optimal parameters (reported in Table 1) leads to an increase in both the wind stress and latent heat by around 24% and 12% respectively. The sensible heat flux is decreased by the combined effect of both the multiplying coefficient of 1.13 and the bias of 8 W m^{-2}. Lastly, precipitation is strongly decreased by nearly a half; the factor applied to the precipitation is quite large but is realistic with regards to the ECMWF ERA-40 and GCPC analyses.

[39] When applied over the POMME domain (Table 2), this leads on average to a comparable decrease in the latent and sensible heat fluxes (−8 W m^{-2}), inducing a decrease of the annual net heat flux of 48%. Nonetheless, the net heat flux remains positive (+17 W m^{-2}). The wind stress is increased by around 24% (+0.027 N m^{-2}). The *E-P* budget undergoes a change of sign: the adjusted evaporation exceeds precipitation, which is due both to the increase in evaporation and to the strong reduction of the precipitation rate (−1.5 mm d^{-1}).

4.2. Optimized One-Dimensional Simulation

[40] The set of optimal parameters was then used to make a new run with the 1-D model (Figures 5 and 6). The evolution of the SST (Figure 5a) is very well reproduced by the model: both the annual cycle, with an amplitude of 8.5°C, and its higher-frequency variability. The mean difference between simulated and observed SST is only 0.02°C with a standard deviation of 0.18°C. Note that the SST evolution is surprisingly similar to that of the *Levitus and Boyer* [1994] climatology, except during the summer months. In contrast, when forced with the original unadjusted fluxes, the 1-D model drifts and the SSTs reach values as high as 26°C, i.e., nearly 3°C higher than the observed maximum in August. This disagreement is a consequence of too weak cooling of the unadjusted fluxes over shallow summer mixed layers.

[41] In contrast with the simulated SSS obtained with the original unadjusted fluxes that has no seasonal cycle and reflects the strong errors associated with excessive precipitation in the freshwater budget, the optimized SSS displays a seasonal cycle with an amplitude of 0.15 psu, in quite good agreement with both the analyses and the *Levitus et al.* [1994] climatology (Figure 5b). Model SSS and analyses differ by an average of 0.02 psu, with a rms of 0.03 psu. The simulation of salinity is however generally less good than that of temperature, namely with a model intraseasonal SSS variability differing perceptibly from that of the analyses. For instance, significant increases of salinity are simulated by the 1-D model in November 2000 and in August 2001. These events, which are mainly due to horizontal Ekman advection, seem to be realistic even if they do not have any equivalent in the analyses. These discrepancies are to be attributed more to errors in both the SSS analyses (poor sampling) and the SSS forcing than to the 1-D model itself. Precipitation rates used to force the 1-D model might indeed not be in phase with real events (see an example of freshening at the end of August in Figure 5b) although corrected in intensity.

[42] The temperature profile (Figure 6a) obtained at the end of the simulation compares quite well with that at P3, implying that the seasonal evolution of the top layers including both winter deepening and spring shoaling is well simulated. For the same reasons as those mentioned above, the salinity profile obtained at the end of the simulation compares less well with P3 than the temperature one (Figure 6b).

[43] The MLD combined with SST and SSS is a good diagnostic for the upper layer stratification. Several criteria were tested on the extended POMME data set, among which those of *Kara et al.* [2000] and *Thomson and Fine* [2003], that are well suited for CTD data. However, a simple criterion of MLD was finally adopted, consisting in a change in density of 0.02 kg m^{-3} relative to the density at the second level of the model (10 m) [*Boyer de Montégut et al.*, 2004]. This criterion was proved to be very well suited for both CTD data and model data used during POMME, for both strongly and weakly stratified layers and over the whole duration of the experiment. The MLD (Figure 5c) varies from less than 25 m in summer to a winter maximum of 185 m in March. Note that the shoaling period is very short (1 month, from mid-March to mid-April) in contrast with the much longer deepening period (5 months and a half, from October to mid-March), leading to an obvious asymmetry in the annual MLD cycle. All these features are in agreement with the annual MLD cycle described a little further south by *Weller et al.* [2004] from observations collected during the Subduction Experiment (June 1991–July 1993). With the unadjusted fluxes, the MLD is largely underestimated almost all along the year. Note also that the MLD deduced from the *Levitus et al.* [1994] climatologies does not reproduce properly the asymmetry of the model annual cycle and is comparatively too weak.

[44] To conclude, the results indicate that the GA leads to a set of model parameters and flux corrections allowing us

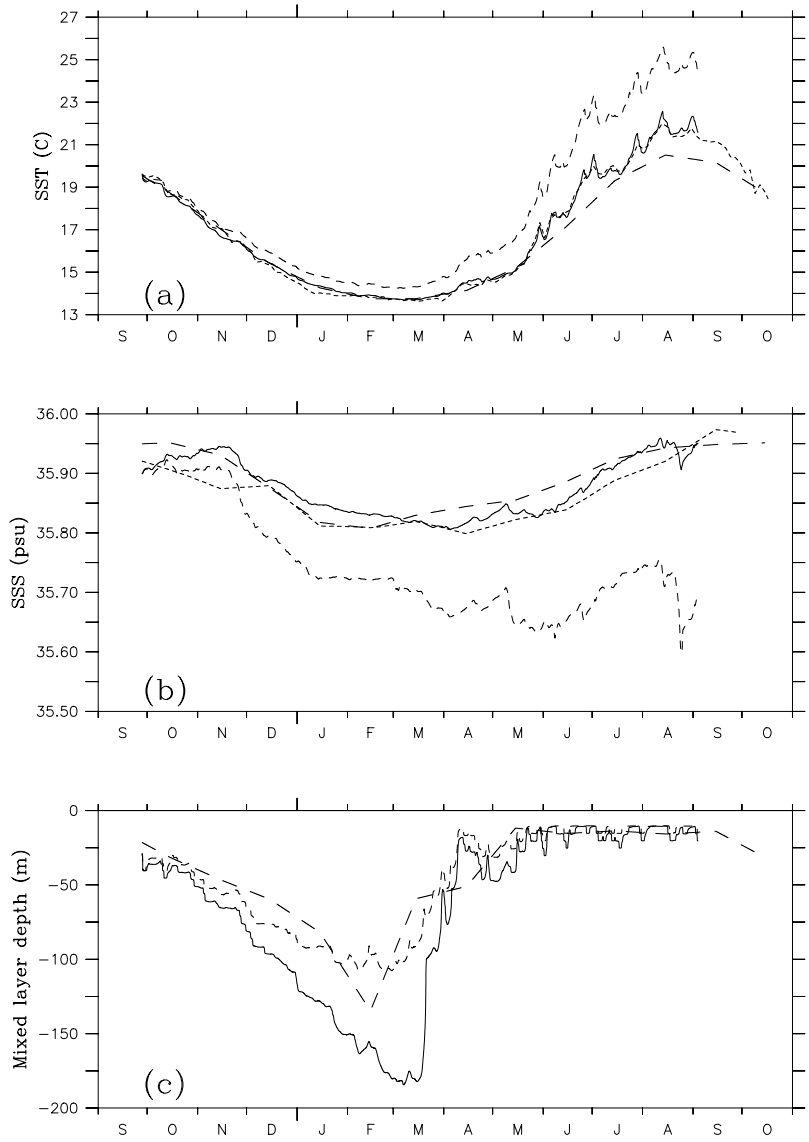

Figure 5. Temporal evolution of (a) sea surface temperature (SST) (deg), (b) sea surface salinity (SSS) (psu), and (c) mixed layer depth (m) simulated by the model forced by the adjusted (solid line) and the unadjusted fluxes (dashed line), deduced from analyses (small dashed line) and from the monthly *Levitus and Boyer* [1994] (SST) and *Levitus et al.* [1994] (SSS) climatologies (long dashed line).

to simulate surprisingly well the evolution of the mean temperature and salinity over the year. This gives a posteriori some confidence not only in the corrections proposed for heat and salt budgets, but also in the hypothesis of the 1-D approach described in this article.

4.3. Adjusted Heat, Salt, and Momentum Budgets

[45] The annual adjusted flux fields are displayed in Figure 7. The most important components of the net heat flux are, by decreasing order: the net shortwave heat, the latent heat, the net longwave heat and finally the sensible heat. The net heat flux (Figure 7e) is negative north of 44.5°N in the western part of the domain, with a marked north to south gradient between 45°N and 43°N. It is positive everywhere else, with quite homogeneous values between 40°N and 38°N.

[46] The annual shortwave heat (Figure 7d) presents a well-known increase from north to south, associated with the astronomical characteristics of the zone. The latent heat (Figure 7b), everywhere negative, has strong latitudinal heterogeneity. Strongly negative in the south because of warmer SST, its amplitude decreases from -80 W m^{-2} (in the most southern part of the domain) to -70 W m^{-2} near 42°N, before increasing again northward of 44°N. Values of -80 W m^{-2} are reached in the northwestern part of the domain due to the strengthening of the winds.

[47] It is clear that the sum of the contributions of the latent heat and shortwave to the net heat flux is not the same throughout the zone. In the northwestern part of the domain, the net heat flux is negative because of a weak solar heat flux and a strong negative latent heat flux. Consequently, the net heat flux rapidly decreases beyond 43°N. In the south, the shortwave heat flux is balanced by the largely negative latent heat flux associated with warm SSTs. The quasi-equilibrium between these two fluxes generates a

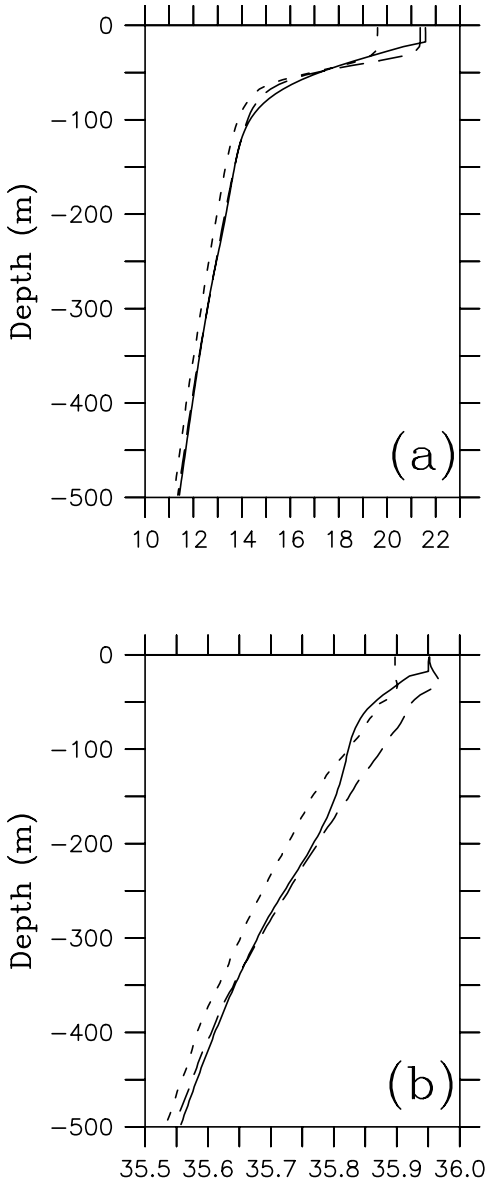

Figure 6. Model (a) temperature and (b) salinity profiles (solid line) compared with domain mean at P0 (model initial state, small dashed line) and P3 (long dashed line).

zone without a notable gradient in the net heat flux field (Figure 7e).

[48] The mesoscale features present in the annual net heat flux (Figure 7e) are due to mesoscale heterogeneities in the latent heat and, in a minor way, in the sensible heat. In both fields, the mesoscale patterns do not reflect the annual mean SST field, which presents quite a regular north to south gradient. These structures primarily come from flux anomalies that were present during specific periods of the year, that is when the turbulent heat fluxes were the strongest, i.e., during fall and winter. These anomalies were generated by the SST distribution, in particular because of its mesoscale heterogeneity. Thus the mesoscale pattern of the annual mean net heat flux directly reflects the winter/fall heterogeneity of SST.

[49] The *E-P* field (Figure 7f) displays a zonal distribution with a marked north to south gradient, from weak values near 44°N to increasingly positive values southward. This distribution reflects the cumulative impacts of increased evaporation over warm waters and decreased precipitation in the south of the domain.

4.4. Impact on the Annual Buoyancy Flux

[50] For subduction, the density flux associated with atmospheric forcing is of particular importance [*Marshall et al.*, 1993]; this flux was thus evaluated for comparison with climatological estimates. The buoyancy flux (F) into the ocean surface is given by the following equation:

$$F = -\frac{\alpha g}{C_p} Q_{\text{net}} + \beta g \rho \frac{S(E-P)}{(1 - S/1000)}, \tag{20}$$

where Q_{net} is the net heat flux and S is the SSS in psu and g the gravity. The density of water at the sea surface (ρ), the specific heat capacity (C_p) and the temperature expansion (α) and haline contraction coefficients (β) have been determined using the classical *Millero et al.* [1973, 1980] equations. This analysis requires the use of a rescaled buoyancy flux (F^*),

$$F^* = -\frac{C_p}{\alpha g} F, \tag{21}$$

that splits into thermal (F_T^*) and saline (F_S^*) contributions:

$$F^* = F_T^* + F_S^*, \tag{22}$$

with

$$F_T^* = Q_{\text{net}} \tag{23}$$

$$F_S^* = -\frac{\beta \rho C_p}{\alpha} \frac{S(E-P)}{(1 - S/1000)}. \tag{24}$$

Note that a heat loss ($Q_{\text{net}} \leq 0$) or net evaporation ($E \geq P$) results in a negative thermal or saline contribution to the rescaled flux F^*.

[51] Seasonal variations of the domain-averaged rescaled flux F^* display an annual cycle with a range of variations of 400 W m^{-2}: the 10 day time filtered series (Figure 8) indicate that the rescaled buoyancy flux is negative from mid-September to March (when spring restratification begins), reaching its minimum in mid-December and its maximum in May–June. This cycle largely reflects the thermal contribution, and has greater variability in winter than in summer. Instantaneous losses of 350 W m^{-2} are reached in winter and maximum gains of 200 W m^{-2} in May–June. On average, the annual rescaled buoyancy flux is positive (+13.0 W m^{-2}), i.e., corresponds to a gain for the ocean, due to an excess of the thermal (+17.0 W m^{-2}) over the freshwater contribution (−4.0 W m^{-2}). Note that the annual freshwater contribution represents nearly a quarter of the annual thermal contribution, even if its instantaneous effect is very weak compared to that of the thermal one. In some specific cases, the buoyancy input from rain may not be so insignificant as it has been shown that the mixed layer depth can shallow rapidly under this effect by several tens of meters [*McCulloch et al.*, 2004].

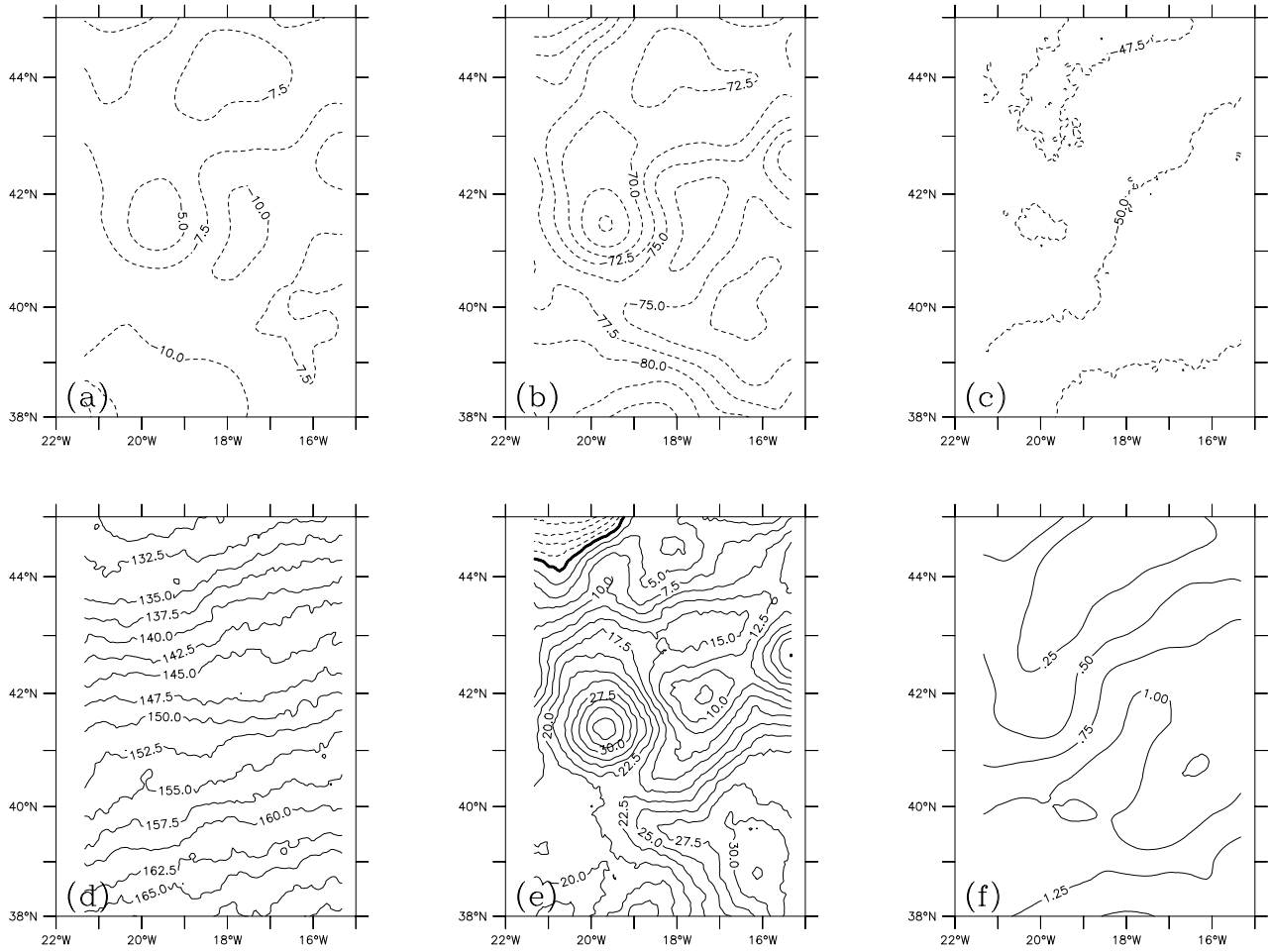

Figure 7. Components of the annual heat fluxes: (a) sensible; (b) latent; (c) net longwave; (d) net shortwave; (e) net heat (W m^{-2}); and (f) *E-P* (mm d^{-1}). Contour intervals are 2.5 W m^{-2} for heat fluxes and 0.25 mm d^{-1} for *E-P*. Period considered is 2 September 2000–2001.

[52] The spatial structure of the annual rescaled buoyancy flux (Figure 9a) displays strong latitudinal and longitudinal heterogeneities, reflecting mainly the structure of the thermal contribution (Figure 9b). The haline contribution (Figure 9c) appears to be quite negligible, except south of 42°N, where the negative haline contribution (net evaporation) reduces the thermal one. Maximum positive values of up to +30 W m^{-2} are located between 40°N and 43°N, confined between much smaller positive values (+15 W m^{-2}) south of 40°N and negative values (down to −15 W m^{-2}) north of 44°N.

5. Conclusions

[53] A method based on a 1-D modeling approach is proposed in this paper to correct the precipitation and surface turbulent fluxes over a 500 × 700 km wide oceanic zone investigated during the POMME experiment. The correction is applied so that the heat, salt and momentum sea surface budgets are in agreement with the mixed layer heat and salt contents deduced from the POMME data set. The 1 year duration of this experiment and the consistent sampling methodology adopted for the 4 hydrographic networks P0 to P3 are particularly appropriate for obtaining an estimate of the ocean top layer evolution and to compute the mean advective terms forcing the permanent thermocline. Eight adjustable parameters are selected, either to tune poorly known constants of the 1-D model or to correct air-sea fluxes. One parameter concerns the parameterization of the penetrative solar radiation (D_2), two the diapycnal mixing parameterization of *Large et al.* [1994] used in the 1-D model, and the last five parameters are corrections applied to the air-sea fluxes (wind stress, latent heat, sensible heat and precipitation). These eight parameters are optimized with a genetic algorithm, which aims to minimize a cost function taking into account the errors between (1) modeled SST and SSS and spatially averaged data issued from independent daily reanalyses; and (2) modeled T and S vertical profiles and spatially averaged profiles obtained from CTD measurements collected during the P1, P2 and P3 hydrographic networks. This optimization makes it possible to derive a set of eight optimal values, and then to obtain a physically realistic 1-year-long simulation with the 1-D model. The flux corrections are then applied to the daily flux fields at each point of the domain. The correction of the annual net heat flux is −16 W m^{-2} for the whole domain, due to underestimated latent and

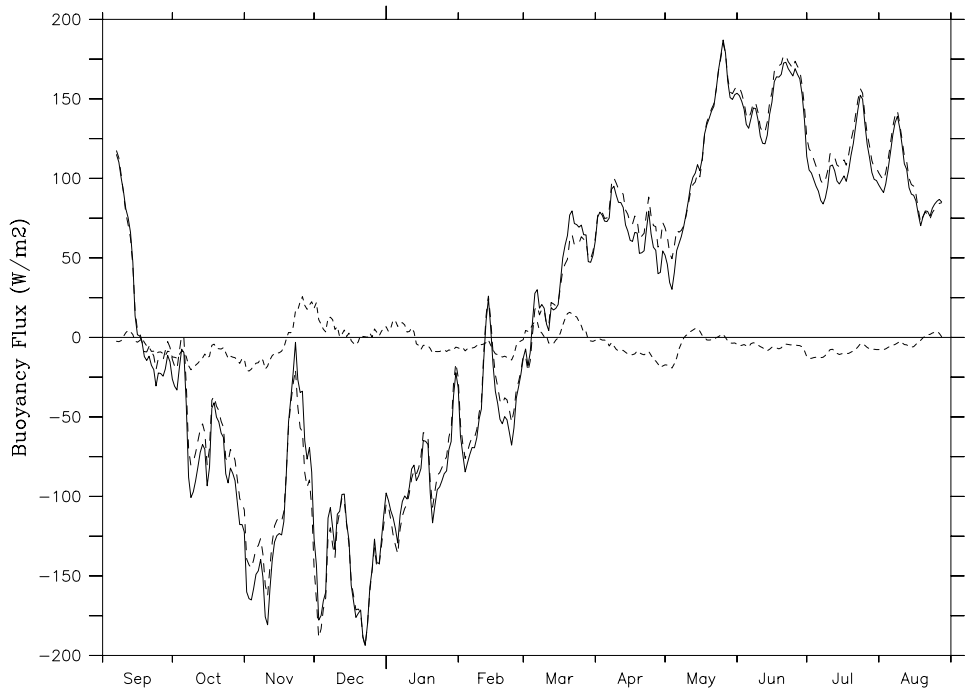

Figure 8. Ten day run averaged time series of the rescaled buoyancy flux (solid line), thermal contribution (long dashed line), and haline contribution (small dashed line) in W m^{-2}.

sensible heat losses (−8 W m^{-2} each). The wind stress is increased by 24%. The correction made on precipitation (a reduction of 44%) reverses the sign of the *E-P* budget which becomes positive, corresponding to an annual net evaporation. Finally, the net adjusted annual buoyancy budget, expressed as a rescaled flux, is +13.0 W m^{-2} for the whole POMME domain, resulting from a positive heat (+17.0 W m^{-2}) and a negative salt (−4.0 W m^{-2}) contribution.

[54] Such a 1-D approach was possible due to the simplicity of the ocean processes taking place in this area of the northeast Atlantic, with weak eddy kinetic energy and mesoscale activity compared to most midlatitude areas. This approach is indeed crucially dependent on temporal and spatial scales and both the 1-D modeling and optimal set of parameters may not be relevant in another region (e.g., the Gulf Stream region) and for other timescales (e.g., climatological timescales). In particular, the set of parameters obtained may vary in time, according to the season: this is particularly the case with the adjusted parameter D_2 used in the radiation parameterization, which may depend on the bloom; this is also probably the case with the diapycnal mixing coefficients, the roles of which are much more important during shoaling and in summer.

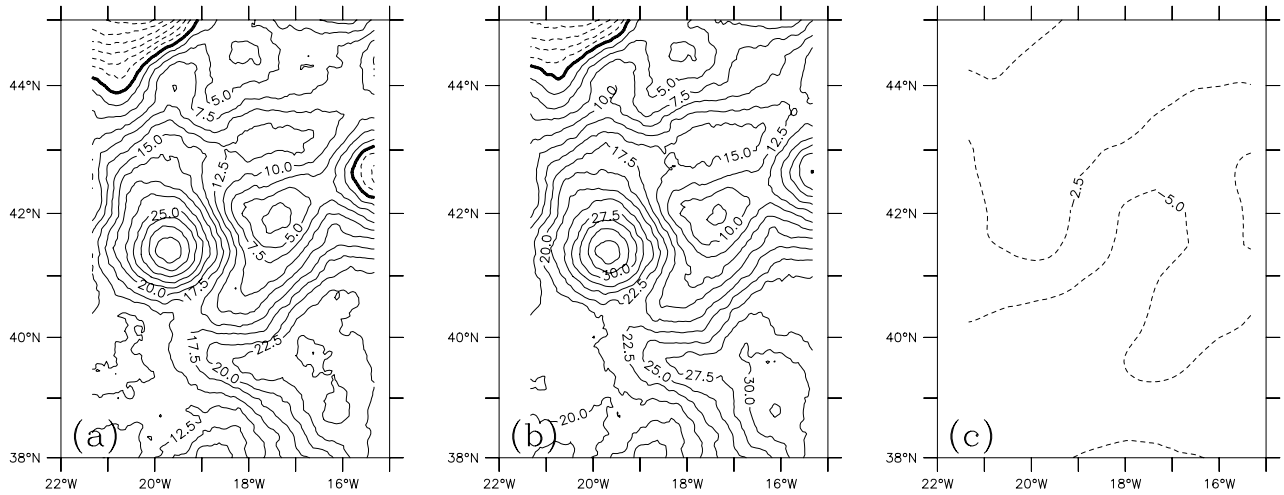

Figure 9. Components of the annual rescaled buoyancy flux expressed in W m^{-2}: (a) total flux; (b) thermal contribution; and (c) haline contribution. Contour intervals are 2.5 W m^{-2}. Period considered is 2 September 2000–2001.

Table 3. Comparison of ARPEGE and European Centre for Medium-Range Weather Forecasts (ECMWF) Models With Adjusted Programme Océan Multidisciplinaire Méso Echelle (POMME) Budgets[a]

Flux	ARPEGE	ECMWF	Adjusted
Shortwave	150.7	134.5	149.7
Longwave	−80.0	−46.4	−49.8
Latent	−98.2	−89.3	−74.7
Sensible	2.4	−8.0	−8.2
Net heat	−25.1	−9.2	17.0
Wind stress	0.130	0.136	0.138
E-P	0.57	−0.30	0.75
P	2.9	3.4	1.9

[a]Domain considered is 21.33°−15.33°W, 38°−45°N. Heat fluxes are in W m^{-2}; wind stress is in N m^{-2}; *E-P* and *P* are in mm d^{-1}. Period considered is 2 September 2000–2001.

[55] When compared with fluxes produced by the ECMWF and the French operational numerical weather prediction ARPEGE model [*Courtier et al.*, 1991], the annual adjusted fluxes averaged over the POMME domain reveal the large discrepancies in the NWP model surface fluxes (Table 3). The ECMWF solar heat flux is underestimated by 15 W m^{-2} and the nonsolar cooling overestimated by 11 W m^{-2} compared to the adjusted fluxes. Both fluxes contribute to an underestimate of the net heat flux by some 26 W m^{-2}. In ARPEGE, the solar heat flux is very close to our estimate. However, the ARPEGE nonsolar cooling is overestimated by 43 W m^{-2} leading to a strong underestimate for the net heat flux of 42 W m^{-2}. The adjusted freshwater flux is positive and differs by 1.05 mm d^{-1} from the ECMWF flux, which is negative (−0.3 mm d^{-1}), and by 0.18 mm d^{-1} from the ARPEGE flux, which is positive (0.57 mm d^{-1}), primarily because of excessive precipitation in the NWP models.

[56] This study also gives important insights into the uncertainties affecting estimates of buoyancy fluxes in climatologies. Despite similarities between the SSTs and SSSs observed during POMME and climatological values of *Levitus and Boyer* [1994] and *Levitus et al.* [1994] (see Figure 5), climatological rescaled buoyancy fluxes obtained by *Marshall et al.* [1993] and *McLaren and Williams* [2001] differ strongly from our results. Both these authors obtain similar zonal distributions of the rescaled buoyancy flux (the spatial patterns are roughly the same as those in the present study, except that mesoscale structures are absent in climatologies) but biases ranging from −20 to −35 W m^{-2} are noted, indicating that the climatologies tend to increase the density of the oceanic top layers. Such large differences are not likely to result from interannual variability anomalies, which can be of the order of less than 10 W m^{-2} according to *McLaren and Williams* [2001]. These discrepancies probably result from an excessive cooling in the climatologies used by *Marshall et al.* [1993] and *McLaren and Williams* [2001] (*Isemer and Hasse* [1987] and *Da Silva et al.* [1994] for the heat fluxes and *Schmitt et al.* [1989] and *Levitus et al.* [1994] for the freshwater fluxes, respectively). This result is largely supported by previous studies by *Moyer and Weller* [1997] and *Weller et al.* [2004].

[57] Our adjusted fluxes have already been used to successfully force three dimensional models for physical studies [*Paci et al.*, 2005; *Giordani et al.*, 2005a, 2005b] and biogeochemical studies [*Lévy et al.*, 2005; S. Roudesli et al., A one-dimensional ecosystem model of the northeast Atlantic Ocean (POMME experiment): Annual cycle, species succession, and biogeochemical fluxes, submitted to *Journal of Geophysical Research*, 2005] over the POMME domain. They also constitute a very important result as the heat budget produced by a statistical model assimilating all the data collected during the POMME experiment [*Gaillard et al.*, 2005] is closed by applying our flux estimates. The success of combining our results with the above studies demonstrates that this work significantly contributes to the production of realistic simulations of the upper ocean.

[58] **Acknowledgments.** We would like to thank Laurent Mémery who, together with Gilles Reverdin, was the scientific leader of the POMME project and also the ship principal scientists Yves Deseaubies and Jérôme Paillet (POMME0), Louis Prieur and Fréderic Herpers (POMME1), Micheline Bianchi and Jérôme Paillet (POMME2), and Jean-Claude Gascard (POMME3). The genetic algorithm used in this study is from David L. Carroll (University of Illinois, 140 Mechanical Engineering Bldg. 1206 W. Green Street, Urbana, IL 61801) and was provided by Fabrice Hernandez (IRD, Toulouse), to whom we are indebted. Special thanks to A. Pirani for greatly improving the English of the manuscript. We also thank two anonymous reviewers and A. Oschlies for their useful comments. This work was supported by funding from "Institut National des Sciences de l'Univers" ("Programme Atmosphère Météorologique Océan Superficiel") and Meteo-France.

References

Arpe, K., and E. Roeckner (1999), Simulation of the hydrological cycle over Europe: Model validation and impacts of increasing greenhouse gases, *Adv. Water Resour.*, *23*, 119–1005.

Barnier, B. (1999), The flux problem seen from below the ocean surface, in *SAF Training Workshop—Ocean and Sea Ice*, EUMETSAT, Darmstadt, Germany.

Barnier, B., L. Siefridt, and P. Marchesiello (1995), Thermal forcing for a global ocean circulation model using three-year climatology of ECMWF analyses, *J. Mar. Syst.*, *6*, 363–380.

Barth, N. H. (1992), Oceanographic experiment design II: Genetic algorithms, *J. Atmos. Oceanic Technol.*, *9*, 434–443.

Behringer, D. W., and H. Stommel (1981), Annual heat gain of the tropical Atlantic computed from subsurface ocean data, *J. Phys. Oceanogr.*, *11*, 1393–1398.

Beranger, K., L. Siefridt, B. Barnier, E. Garnier, and H. Roquet (1999), Evaluation of operational ECMWF surface freshwater fluxes over oceans during 1991–1997, *J. Mar. Syst.*, *22*, 13–36.

Blanc, T. V. (1985), Variation of bulk-derived surface flux, stability, and roughness results due to the use of different transfer coefficient schemes, *J. Phys. Oceanogr.*, *15*, 650–669.

Boyer de Montégut, C., G. Madec, A. S. Fischer, A. Lazar, and D. Iudicone (2004), Mixed layer depth over the global ocean: An examination of profile data and a profile-based climatology, *J. Geophys. Res.*, *109*, C12003, doi:10.1029/2004JC002378.

Brisson, A., P. Le Borgne, A. Marsouin, and T. Moreau (1994), Surface irradiances calculated from METEOSAT sensor data during SOFIA-ASTEX, *Int. J. Remote Sens.*, *15*, 197–203.

Caniaux, G., and S. Planton (1998), A three-dimensional ocean mesoscale simulation using data from the SEMAPHORE experiment: Mixed layer heat budget, *J. Geophys. Res.*, *103*, 25,081–25,099.

Caniaux, G., A. Brut, D. Bourras, H. Giordani, A. Paci, L. Prieur, and G. Reverdin (2005), A 1 year sea surface heat budget in the northeastern Atlantic basin during the POMME experiment: 1. Flux estimates, *J. Geophys. Res.*, *110*, C07S02, doi:10.1029/2004JC002596.

Carroll, D. L. (1996), Genetic algorithms and optimizing chemical oxygen-iodine lasers, in *Developments in Theoretical and Applied Mechanics*, vol. XVIII, edited by H. B. Wilson et al., pp. 411–424, Sch. of Eng. Univ. of Ala., Tuscaloosa.

Courtier, P., C. Freydier, J. F. Geleyn, F. Rabier, and M. Rochas (1991), The ARPEGE project at Météo-France, in *ECMWF 1991 Seminar Proceedings: Numerical Methods in Atmospheric Models, ECMWF, 9–13 September 1991*, vol. 2, pp. 123–231, Eur. Cent. for Medium-Range Weather Forecasts, Reading U. K.

Curry, J. A., C. A. Clayson, W. B. Rossow, R. Reeder, Y. C. Zhang, P. J. Webster, G. Liu, and R. S. Sheu (1999), High-resolution satellite-derived

dataset of the surface fluxes of heat, freshwater, and momentum for the TOGA COARE IOP, *Bull. Am. Meteorol. Soc.*, *80*, 2059–2080.

Cushman-Roisin, B. (1987), *Dynamics of the Oceanic Surface Mixed Layer*, edited by P. Muller and D. Henderson, Hawaii Inst. of Geophys., Honolulu.

Da Silva, A. M., C. C. Young, and S. Levitus (1994), *Atlas of Surface Marine Data 1994*, vol. 1, *Algorithms and Procedures*, *NOAA Atlas NESDIS 6*, 83 pp., Natl. Oceanic and Atmos. Admin., Silver Spring, Md.

Ducet, N., P. Y. Le Traon, and G. Reverdin (2000), Global high-resolution mapping of ocean circulation from TOPEX/Poseidon and ERS-1 and -2, *J. Geophys. Res.*, *105*, 19,477–19,489.

Eymard, L., et al. (1999), Surface fluxes in the North Atlantic Current during the CATCH/FASTEX experiment, *Q. J. R. Meteorol. Soc.*, *125*, 3563–3599.

Gaillard, F., H. Mercier, and C. Kermabon (2005), A synthesis of the POMME physical data set: One year monitoring of the upper layer, *J. Geophys. Res.*, *110*, C07S07, doi:10.1029/2004JC002764.

Gaspar, P., Y. Grégoris, and J. M. Lefèvre (1990), A simple eddy kinetic energy model for simulations of the oceanic vertical mixing: Tests at station Papa and long-term upper ocean study site, *J. Geophys. Res.*, *95*, 179–193.

Gill, A. E. (1982), *Atmosphere-Ocean Dynamics*, 662 pp., Elsevier, New York.

Giordani, H., G. Caniaux, and L. Prieur (2005a), A simplified 3D oceanic model assimilating geostrophic currents: Application to the POMME experiment, *J. Phys. Oceanogr.*, *35*, 628–644.

Giordani, H., G. Caniaux, L. Prieur, A. Paci, and S. Giraud (2005b), A 1 year mesoscale simulation in the northeast Atlantic: Mixed layer heat and detrainment budgets during the POMME experiment, *J. Geophys. Res.*, doi:10.1029/2004JC002765, in press.

Grist, J. P., and S. A. Josey (2003), Inverse analysis adjustment of the SOC air-sea flux climatology using ocean heat transport constraints, *J. Clim.*, *16*, 3274–3295.

Holland, J. (1975), *Adaptation in Natural and Artificial Systems*, Univ. of Mich. Press, Ann Arbor.

Holton, J. R. (1992), *An Introduction to Dynamic Meteorology*, 3rd ed., 511 pp., Elsevier, New York.

Isemer, H. J., and L. Hasse (1987), *The Bunker Climate Atlas of the North Atlantic Ocean*, vol. 2, 252 pp., Springer, New York.

Isemer, H. J., J. Willebrand, and L. Hasse (1989), Fine adjustment of large scale air-sea energy flux parameterizations by direct estimates of ocean heat transport, *J. Clim.*, *2*, 1173–1184.

Jerlov, N. G. (1974), A simple method for measuring quanta irradiance in the ocean, *Rep. 24*, Kobenhavn Univ. Inst. Fysik Oceanogr., Germany.

Jerlov, N. G. (1976), *Marine Optics*, *Elsevier Oceanogr. Ser.*, vol. 14, 231 pp., Elsevier, New York.

Josey, S. A., E. C. Kent, and P. K. Taylor (1999), New insights into the ocean heat budget closure problem from analysis of the SOC air-sea flux climatology, *J. Clim.*, *12*, 2856–2880.

Kantha, L. H., and C. A. Clayson (1994), An improved mixed layer model for geophysical applications, *J. Geophys. Res.*, *99*, 25,235–25,266.

Kara, A. B., P. A. Rochford, and H. E. Hurlburt (2000), An optimal definition for ocean mixed layer depth, *J. Geophys. Res.*, *105*, 16,803–16,821.

Large, W. G., J. C. McWilliams, and S. Doney (1994), Ocean vertical mixing: A review and a model with a nonlocal boundary layer parameterization, *Rev. Geophys.*, *32*, 363–403.

Ledwell, J. R., A. J. Wilson, and C. S. Low (1993), Evidence for slow mixing across the pycnocline from an open-ocean tracer-release experiment, *Nature*, *364*, 701–703.

Levitus, S., and T. P. Boyer (1994), *World Ocean Atlas 1994*, vol. 4, *Temperature*, *NOAA Atlas NESDIS 4*, 129 pp., Natl. Oceanic and Atmos. Admin., Silver Spring, Md.

Levitus, S., R. Burgett, and T. P. Boyer (1994), *World Ocean Atlas 1994*, vol. 3, *Salinity*, *NOAA Atlas NESDIS 3*, 111 pp., Natl. Oceanic and Atmos. Admin., Silver Spring, Md.

Lévy, M., M. Gavart, L. Mmery, G. Caniaux, and A. Paci (2005), A four-dimensional mesoscale map of the spring bloom in the northeast Atlantic (POMME experiment): Results of a prognostic model, *J. Geophys. Res.*, *110*, C07S21, doi:10.1029/2004JC002588.

Macdonald, A. M., and C. Wunsch (1996), An estimate of global ocean circulation and heat fluxes, *Nature*, *382*, 436–439.

Marshall, J. C., A. J. G. Nurser, and R. G. Williams (1993), Inferring the subduction rate and period over the North Atlantic, *J. Phys. Oceanogr.*, *23*, 1315–1329.

McCulloch, M. E., and H. Leach (1998), Air sea fluxes inferred from an upper ocean heat budget north-east of the Azores, *Q. J. R. Meteorol. Soc.*, *124*, 2465–2476.

McCulloch, M. E., J. O. S. Alves, and M. J. Bell (2004), Modelling shallow mixed layers in the northeast Atlantic, *J. Mar. Syst.*, *52*, 107–119.

McLaren, A. J., and R. G. Williams (2001), Interannual variability in the thermodynamics of subduction over the North Atlantic, *J. Phys. Oceanogr.*, *31*, 3284–3294.

Mémery, L., G. Reverdin, J. Paillet, and A. Oschlies (2005), Introduction to the POMME special section: Thermocline ventilation and biogeochemical tracer distribution in the northeast Atlantic Ocean and impact of mesoscale dynamics, *J. Geophys. Res.*, doi:10.1029/2005JC002976, in press.

Millero, F. J., G. Perron, and J. E. Desnoyers (1973), The heat capacity of sea-water solutions from 5 to 35°C and 0.5 to 22‰ chlorinity, *J. Geophys. Res.*, *78*, 4499–4507.

Millero, F. J., C.-T. Chen, A. Bradshow, and K. Schleicher (1980), A new high-pressure equation of state for sea-water, *Deep Sea Res., Part A*, *27*, 255–264.

Moyer, K. A., and R. A. Weller (1997), Observations of surface forcing from the subduction experiment: A comparison with global model products and climatological datasets, *J. Clim.*, *10*, 2725–2742.

Paci, A., G. Caniaux, M. Gavart, H. Giordani, M. Lévy, L. Prieur, and G. Reverdin (2005), A high-resolution simulation of the ocean during the POMME experiment: Simulation results and comparison with observations, *J. Geophys. Res.*, doi:10.1029/2004JC002712, in press.

Paulson, C. A., and J. J. Simpson (1977), Irradiance measurements in the upper ocean, *J. Phys. Oceanogr.*, *7*, 952–956.

Peters, H., M. C. Gregg, and J. M. Toole (1988), On the parameterization of equatorial turbulence, *J. Geophys. Res.*, *93*, 1199–1218.

Prieur, L., and L. Legendre (1988), Oceanic criteria for new phytoplankton production, in *Toward a Theory on Biological-Physical Interactions in the World Ocean*, edited by B. J. Rothschild, pp. 71–112, Elsevier, New York.

Qiu, B., and R. X. Huang (1995), Ventilation of the North Atlantic and North Pacific: Subduction versus obduction, *J. Phys. Oceanogr.*, *25*, 2374–2390.

Reverdin, G., M. Assenbaum, and L. Prieur (2005), Eastern North Atlantic Mode Waters during POMME, *J. Geophys. Res.*, doi:10.1029/2004JC002613, in press.

Schmitt, R. W., P. S. Bogden, and C. E. Dorman (1989), Evaporation minus precipitation and density fluxes for the North Atlantic, *J. Phys. Oceanogr.*, *19*, 1208–1221.

Simonot, J. Y., and H. Le Treut (1986), A climatological field of mean optical properties of the world ocean, *J. Geophys. Res.*, *91*, 6642–6646.

Thomson, R. E., and I. V. Fine (2003), Estimating mixed layer depth from oceanic profile data, *J. Atmos. Oceanic Technol.*, *20*, 319–329.

Trenberth, K. E. (1997), Using atmospheric budgets as a constraint on surface fluxes, *J. Clim.*, *10*, 2796–2809.

Weller, R. A., P. W. Furey, M. A. Spall, and R. E. Davis (2004), The large-scale context for oceanic subduction in the northeast Atlantic, *Deep Sea Res., Part I*, *51*, 665–699.

WGASF Group (2000), Intercomparison and validation of ocean-atmosphere energy flux fields, final report, 305 pp., Joint WCRP/SCOR Working Group on Air-Sea Fluxes, World Meteorol. Organ., Geneva, Switzerland.

S. Belamari, G. Caniaux, H. Giordani, and A. Paci, Centre National de Recherches Météorologiques, 42 avenue G. Coriolis, F-31057 Toulouse Cedex, France. (sophie.belamari@meteo.fr; caniaux@meteo.fr; herve.giordani@meteo.fr; alexandre.paci@meteo.fr)

L. Prieur, Laboratoire d'Océanographie de Villefranche-sur-mer, BP08, F-06230 Villefranche-sur-mer, France. (prieur@obs-vlfr.fr)

G. Reverdin, Laboratoire d'Océanographie et du Climat: Expérimentation et Approche Numérique, Institut Pierre Simon Laplace, 4, place Jussieu, F-75252 Paris Cedex 05, France. (reverdin@lodyc.jussieu.fr)